electronics

Article

Proactive Power Compensation Strategy of Pulsed Load for Transient Ride-Through of Ship Microgrid

Yue Ding , Ke Zhao *, Jiandong Duan and Li Sun

School of Electrical Engineering and Automation, Harbin Institute of Technology, Harbin 150001, China; 20b906052@stu.hit.edu.cn (Y.D.)
* Correspondence: zhaoke@hit.edu.cn

Abstract

A proactive power compensation strategy applicable to achieving transient ride-through of ship microgrid (SM) under pulsed load is presented in this paper. The essence of this strategy can be summarized as the generator enters a transient process when a large portion of the pulsed load is connected to the islanded microgrid. Next, the pulsed load power is calculated and predicted over a 20 ms time scale based on the changes in stator current, stator voltage, excitation current and excitation voltage during the process. As a result, the predicted power is used as the control desired value of the compensation device to ensure that the microgrid recovers the power balance and achieves transient ride-through. Finally, the proposed control strategy not only replaces the one machine infinite bus (OMIB) with the transient model of the SG but also utilizes the energy storage device to actively guide the generator to output the differential power in the microgrid. The power response time of the compensation system is in the range of 6–20 ms, which is able to realize the transient ride-through of the SG within one cycle.

Keywords: pulsed load; power prediction; power compensation; power compensation; transient ride-through

check for updates

Academic Editor: Dorin Petreus

Received: 4 November 2025
Revised: 22 November 2025
Accepted: 24 November 2025
Published: 27 November 2025

Citation: Ding, Y.; Zhao, K.; Duan, J.; Sun, L. Proactive Power Compensation Strategy of Pulsed Load for Transient Ride-Through of Ship Microgrid. *Electronics* **2025**, *14*, 4665. https://doi.org/10.3390/electronics14234665

1. Introduction

The increasing severity of the global environmental and energy issues has made ocean development an important way to address the crisis [1]. Therefore, the study of the stability of SM has become the most critical aspect to help marine development. The operational status and environment of SM make them typical small-capacity islanded microgrids [2]. For instance, the diesel engine has been widely used in the oil extraction industry. The capacity of this engine is relatively small, so multiple units are usually connected in parallel to construct a microgrid [3]. The SM not only has to provide electricity for motors but also take care of the living electricity for the operators. Diesel generator (DG) has been widely used in SM. However, the access to a large number of new power electronic loads causes a change in the electrical characteristics of SM. Among the above power electronic loads, the most typical and harmful ones are pulsed load.

The diesel engine (DE) is the power source of the SM and is connected to the synchronous generator through the crankshaft. The ECU (Electronic Control Unit) implements speed tracking control in addition to a healthy AFR (Air Fuel Ratio) [4]. However, the abnormal combustion characteristics of diesel engines such as misfire and deflagration in low and high load intervals make the diesel engine require high accuracy in speed control. Ref. [5] studied the combustion and emission characteristics of the diesel engines, and its results showed that the DE can rely on higher combustion activity to adapt to pulsed load. Same as this, the advantages of diesel generators under the pulsed load conditions are similarly described in [6]. Secondly, the mentioned microgrid has different scales for the time of attention of the connected loads compared to the traditional grid. In power system transient analysis, static composite load model and OMIB model have been widely used in large power grids. For instance, researchers categorize load on a bus into active and reactive load based on their static characteristics. Although [7] analyzes the voltage regulation, frequency restoration and active power characteristics of IEEE 4BUS networks, it is still concerned with static characteristics of microgrids. Similarly, the transient stability problem of voltage source inverter and virtual synchronous machines has been analyzed in [8,9]; both have chosen the single machine infinity model as well as static power characteristics. Ref. [10] has analyzed the dynamic characteristics of distributed microgrids, and although the authors distinguish between loads based on symmetric and asymmetric perspectives, they are still essentially static loads. Traditional grids focus on static stability and the essential reason for such an analysis is that the modeling process assumes grid voltage stability. In other words, this assumption is valid provided that the excitation system of the generator has a strong enough regulation to ensure that the grid has the same steady state and transient processes. It is clear that the pulsed load made the mentioned microgrid no longer have constant voltage and frequency during transients. Therefore, the above assumptions no longer apply for this microgrid. It should be noted that for special industries such as SM, the most important objective is to ensure the rated operation of pulsed loads. Therefore, the conflict between diesel generator and pulsed loads becomes a challenge that must be faced for the stable operation of the aforementioned microgrid.

The current strategies for resolving the conflict can be categorized into two aspects from the "power" point of view. The first is to increase the generating unit capacity or increase their numbers. This method essentially reduces the ratio of pulsed loads to microgrid capacity by increasing microgrid capacity. This method explains why generating unit shutdowns due to impact loads are rarely observed in conventional power grids. For instance, the grid can still operate stably even if a localized three-phase short circuit occurs as a pulsed load [11]. The last is to configure the energy storage device as a source for power compensation. This method takes advantage of the fast power response of power electronic devices to achieve power matching between the source and the pulsed load. Current source converter (CSC) was the first to appear and be used in power compensation devices. Ref. [12] proposed current droop control for CSC, in addition to the detection method of grid impedance to realize the state judgment of the grid, aiming to achieve system stability during the state switching process of the grid. Although the control direction of current source converter and voltage source converter is to ensure the stability of the microgrid system, their respective focuses are not the same. The former mainly inputs power into the microgrid to maintain its power balance, while the latter not only maintains the power balance but also realizes the frequency and voltage support of the microgrid. In [13,14], voltage source converter (VSC) is used as distributed power sources to build a microgrid. The VSCs realize voltage and frequency stabilization through droop control in the microgrid. The effect of line impedance on the control performance of VSC is discussed in these references. As a result, the lack of inertia in the VSC as a power electronic device leads to too fast a response to any excitation. Therefore, the virtual synchronous generator (VSG) has been proposed to address and improve this weakness, and two research directions for VSG are mentioned in Refs. [15,16]. One is a control algorithm for a single VSG and the other is a coordinated control strategy for multiple units. Similarly, the control goals of all the above VSGs focus on frequency robustness as well as voltage robustness. The development of VSG technology enables the application of grid-forming converters in the field of power compensation. In [17], an improved adaptive integrated control strategy is proposed for VSG grid-connected photovoltaic power system, and it is used to suppress harmonics current and power oscillations. Behera Sameer K. et al. acquired the phase information necessary for VSG control by 30 ms adaptive learning law. In [18], Wang MY et al. proposed an accurate small-signal model and grid impedance identification method for VSG inverters. In addition, an improved VSG control with adaptive grid impedance is proposed based on the knowledge of small-signal model and system impedance. However, the FFT calculation of the grid impedance takes several minutes to complete in practical applications. A comparison of the research directions and theoretical models of the above references is shown in Table 1.

Table 1. Comparison with state-of-the-art microgrid analysis models.

Serial Number	Control Strategy	OMIB	Unit Configuration	Control Variable	Response Time	Stability Margin	Energy Storage Requirement
[12]	CSC	Yes	Double CSC	Grid-Forming Current	80–120 ms	PM = 90 deg	Not Mentioned
[13]	VSC	Yes	Single bus + VSG	Bus Voltage	380 ms	Nyquist Stabilization	1250 MW/ 11 mF
[14]	Voltage Droop VSC	Yes	Double VSC	Feeders Impedances	Not Mentioned	Root Trajectory	3–6 kW/DC Power Supply
[15]	MPC-VSG	Yes	Single bus + VSG	Frequency	Not Mentioned	Not Mentioned	20 kW/ 60 kWh Battery
[16]	VSG	Yes	Single bus + VSG	RoCoF	600 ms	Power angle stabilization	50 kW/DC Power Supply
[19]	VSG	Yes	Single bus + VSG	Frequency	300 ms	Root Trajectory	45 kW/DC Power Supply
[20]	Feedforward VSG	Yes	Double VSG	Active Power	Not Mentioned	PM = 90 deg	40 kW/4 uF
[21]	Coordinated VSG	Yes	Four VSG	Active Power	50–100 ms	Not Mentioned	10 kW/4 mF
[22]	VSG	Yes	Single bus + Four VSG	Voltage/Frequency	80–100 ms	Nyquist Stabilization	11 kW/DC Power Supply
[23]	Centralized MPC	Yes	IEEE 39-Bus systems	Frequency	4–220 ms	Not Mentioned	Simulation
This paper	Traditional VSG	No	Double SG + Double AVR	Excitation system and Stator Current Voltage	6–20 ms	Not Mentioned	30 kW/ 100 kWh Battery

Summarizing these references, it can be concluded as follows: (1) the OMIB is used to describe the microgrid to which the above-mentioned converters are accessed. In other words, this means that the bus can be equated to a synchronous generator containing an infinitely large inertia rotor and an infinitely large capacity excitation; (2) energy storage devices and converters are used as generators for microgrids, and both VSG and droop control are based on frequency change for power allocation. However, with frequency as a generator parameter under electromechanical time scale, it is difficult to characterize the transient behavior of microgrid under pulsed load; (3) both VSG and droop control essentially passively regulate their own output power in response to changes in frequency, in addition to both regulating based on steady state power allocation; (4) there is little mention of the exit power compensation process in the references. Since the capacity of the energy storage device is limited, the power compensation must be exited before the energy is exhausted without affecting the stability of the microgrid.

The work and contributions of this paper are summarized below:

(1) A transient model of the generator is used instead of the OMIB. The model includes the transient characteristics of the AVR, as well as the electromagnetic characteristics of the generator stator and rotor.

(2) The transient model was used to calculate and predict the parameters of the pulsed load, and the prediction time scale of less than 20 ms.
(3) The shorter response time of the energy storage to proactively direct the generator to take up the differential power of the SM.

This rest of this paper is organized as follows. Section 2 describes the structure of the microgrid and the problem to be studied, and establishes a transient model of the generator and a generalized model of the compensation system. Compensation strategy for pulsed load and the connotation of transient ride-through in microgrids is elucidated and described in Section 3. In Section 4, an experimental platform is built to verify the correctness and effectiveness of the model and compensation strategy. Finally, the work of this paper is summarized and conclusions are made about the research in this paper in Section 5.

2. Description of the Problem and Model

The microgrid structure applicable to the oil extraction industry studied in this paper is shown in Figure 1. Part I is the energy input component of the microgrid, which contains two electrically excited synchronous generators, two asynchronous motors and two inverters. The desired value of speed tracking control is set by the synchronization device. The inverters and motors are responsible for emulating the speed characteristics of the natural gas engine. Part II is a pulse load compensation device, and includes a supercapacitor energy storage device and a VSG. Part III is the pulsed load, which is an asynchronous motor driven by an inverter.

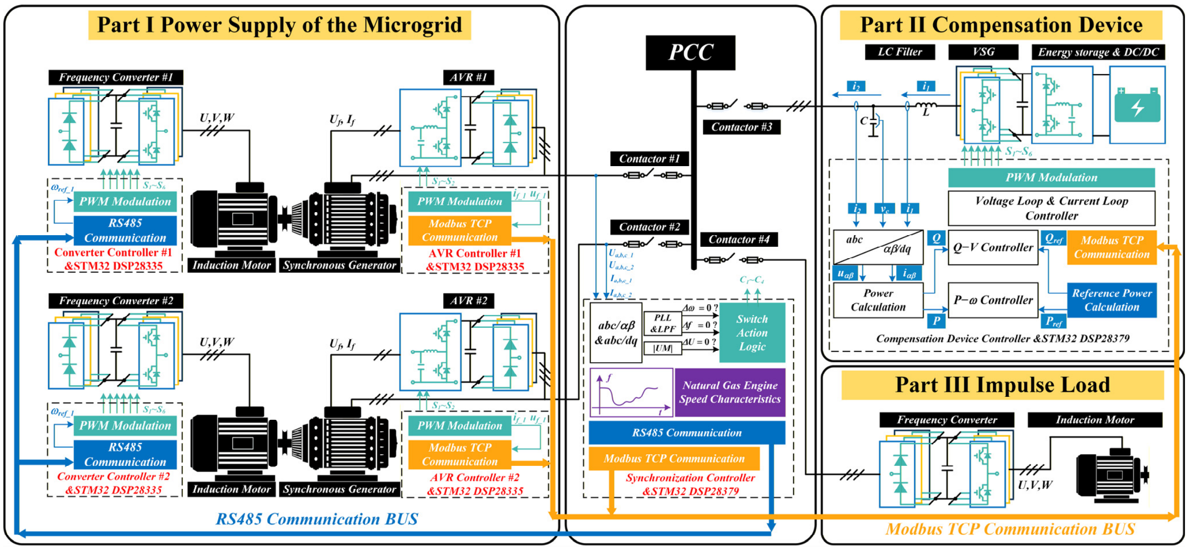

Figure 1. The structure of the SM and its constituent units.

2.1. Physical Description of the Loading Process

As shown in Figure 1, there is only one voltage level at the bus in the microgrid proposed in this paper for the oil extraction industry, while there is almost no equipment such as power transformers in the microgrid. The single voltage level made it easier to quantitatively describe the physical processes of the microgrid under pulsed load, and the processes are as follows.

Firstly, a large proportional pulsed load will not only cause the stator current to increase rapidly but will also cause the rotating magnetic field kinetic potential generated by the stator current to increase rapidly as well. Subsequently, the magnetic chains generated by these rapidly increasing magnetic potentials must also turn chain the excitation winding. As a result, a corresponding current must be induced in the excitation winding according to the principle of conservation of the magnetic chain. Therefore, analyzed on a time scale, this change in magnetic field is the fastest response of the system to the pulsed load. These physical processes are shown in Figure 2.

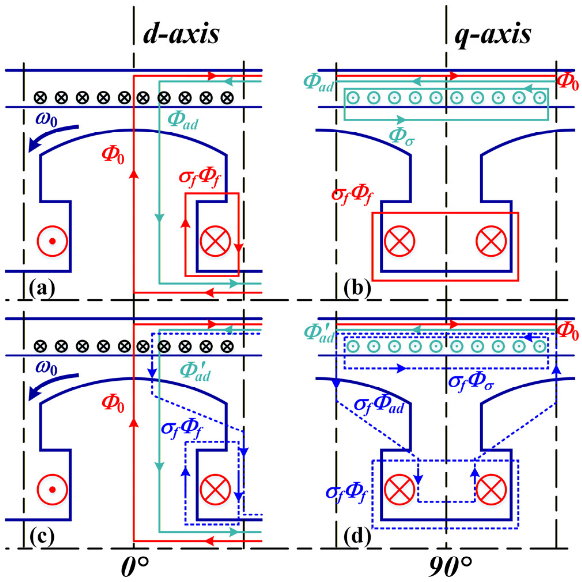

Figure 2. Magnetic flux during loading of the SG. (**a**) d-axis flux before pulsed load. (**b**) q-axis flux before pulsed load. (**c**) d-axis flux after pulsed load. (**d**) q-axis flux after pulsed load.

Figure 2a,b shows the magnetic circuit of the transient armature reaction flux (ϕ'_{ad}), and its mathematical description is as follows:

$$\Delta\phi_0 + \Delta\phi_{f\sigma} + \Delta\phi_{ad} = 0 \tag{1}$$

Define

$$\phi'_{ad} \triangleq \Delta\phi_{ad} = -(\Delta\phi_0 + \Delta\phi_{f\sigma}) \tag{2}$$

Bringing (1) into (2), the solution is as follows:

$$\phi'_{ad}\Big|_{t=0^-} = -i_{f\alpha}/N_f(R_{f\sigma} + R_{ad}) \text{ and } \phi'_{ad}\big|_{t\to\infty} = i_{ad}/N_a R_{ad} \tag{3}$$

where $\Delta\phi_0$ and $\Delta\phi_{f\sigma}$ represent the main flux and leakage flux generated by the current $i_{f\alpha}$, respectively. $\Delta\phi_{ad}$ and ϕ_{ad} stand for the transient and steady state armature reaction flux. N_a and N_f are the turns of the stator and excitation winding. i_{ad} is the d-axis current of stator. R_{ad} and $R_{f\sigma}$ denote the magnetoresistance of the corresponding magnetic circuit in Figure 2c,d, respectively.

In a transient magnetic circuit, the stator current increases rapidly, and at the same time, the current also produces a large armature reaction flux. However, the induced current in the excitation winding prevents the armature reaction flux from passing through itself and forces the armature reaction flux to take a leakage path. Hence, there are two inductive reactance x'_{ad} and x_{ad} throughout the transient process, and their mathematical descriptions are as follows:

$$x'_{ad} \propto \Lambda'_{ad} = 1/(R_{ad} + R_{f\sigma}) \text{ and } x_{ad} \propto \Lambda_{ad} = 1/R_{ad}. \tag{4}$$

These two reactance imply the beginning and end of the transient process, such that

$$x'_{ad} \to x_{ad} \text{ as } t \to \infty. \tag{5}$$

Therefore, this reactance variation not only illustrates the impact of impact loads on the electromagnetic characteristics of the generator but also represents a breakthrough to realize load prediction and transient power compensation.

2.2. Mathematical Description of the Loading Process

Based on the physical description in the previous section, its more detailed mathematical analysis is shown in this section. Meanwhile, the assumptions for the analysis in this section are as follows:

A1: This study is based on a low power generator set, so the effect of damping windings is ignored.

A2: The whole transient process does not take into account the change in generator speed.

The time-domain equation of the generator is shown in (6).

$$\begin{cases} u_d = -R_a i_d + \dot{\psi}_d - \psi_q \\ u_q = -R_a i_q + \dot{\psi}_q + \psi_d \\ u_f = R_f i_f + \dot{\psi}_f \\ \psi_d = -x_d i_d + x_{ad} i_f \\ \psi_q = -x_q i_q \\ \psi_f = -x_{ad} i_d + x_f i_f \end{cases} \tag{6}$$

where $u_{d,q}$, $i_{d,q}$, $x_{d,q}$ represent the stator voltage, current and inductive reactance in the *d*-*q* coordinate system, respectively. u_f, i_f, x_f stand for the excitation voltage, current and reactance. $\Psi_{d,q,f}$ are the magnetic chain of stator windings and the excitation windings. R_a and R_f represent the stator resistance and the excitation winding resistance, respectively.

To solve for the transient current component, rewrite (6) as Laplace's equation. In addition, the rewritten equation is split into voltage, magnetic chain and excitation current equations as follows:

$$\begin{cases} U_d(s) = -R_a I_d(s) + s(\Psi_d(s) - \psi_{d0}) - \Psi_q \\ U_q(s) = -R_a I_q(s) + s(\Psi_q(s) - \psi_{q0}) + \Psi_d \end{cases} \tag{7}$$

$$\begin{cases} \Psi_d(s) = -x_d I_d(s) + x_{ad} I_f(s) \\ \Psi_q(s) = -x_q I_q(s) \end{cases} \tag{8}$$

$$I_f(s) = (U_f(s) + \Psi_{f0} + s x_{ad} I_d(s))/(R_f + s x_f) \tag{9}$$

Bringing (9) into (8) and simplifying to (10), we obtain the following:

$$\begin{aligned} \Psi_d(s) &= -x_d I_d(s) + x_{ad} \frac{(U_f(s) + \Psi_{f0} + s x_{ad} I_d(s))}{(R_f + s x_f)} \\ &= \frac{x_{ad}}{R_f + s x_f}(U_f(s) + \Psi_{f0}) - (x_d - \frac{s x_{ad}^2}{R_f + s x_f}) \cdot I_d(s) \\ &= G(s)(U_f(s) + \Psi_{f0}) - X_d(s) I_d(s) \end{aligned} \tag{10}$$

where $X_d(s)$ is d-axis operational reactance, and its physical implications are consistent with (4), such that

$$\lim_{t \to 0, s \to \infty} X_d(s) = x'_d \text{ and } \lim_{t \to \infty, s \to 0} X_d(s) = x_d. \tag{11}$$

Then, the initial and steady state values of the transient current are calculated individually. Rewriting (7)–(9) into transient component form, the rewritten form is as follows:

$$\begin{cases} -u_{d0}/s = -R_a \Delta I_d(s) + s\Delta\Psi_d(s) - \Delta\Psi_q \\ -u_{q0}/s = -R_a \Delta I_q(s) + s\Delta\Psi_q(s) + \Delta\Psi_d \\ \Delta\Psi_d(s) = -X_d(s)\Delta I_d(s) \\ \Delta\Psi_q(s) = -x_q \Delta I_q(s) \\ \Delta I_f(s) = x_{ad}\Delta I_d(s)/x_f \end{cases} \tag{12}$$

where Δ is the difference between the transient values of each parameter at the moments before and after loading. Simplifying (12) to solve for the $\Delta I_d(s)$ and $\Delta I_q(s)$ produces the following:

$$\begin{cases} \Delta I_d(s) = \frac{(R_a+sx_q)u_{d0}+x_q u_{q0}}{s\{[sX_d(s)+R_a](R_a+sx_q)+X_d(s)x_q\}} \\ \Delta I_q(s) = \frac{[R_a+sX_d(s)]u_{q0}-X_d(s)u_{d0}}{s\{[sX_d(s)+R_a](R_a+sx_q)+X_d(s)x_q\}} \end{cases} \quad (13)$$

Assuming that the impedance R_a and R_f are equal to zero, which also means that there is no attenuation of these free components, and therefore substituting $X_d(s) = x'_d$ into Equation (13), the simplified result is as follows:

$$\Delta I_d(s) = \frac{su_{d0} + u_{q0}}{s(s^2+1)x'_d} \text{ and } \Delta I_q(s) = \frac{su_{q0} - u_{d0}}{s(s^2+1)x_q} \quad (14)$$

Also bringing (14) into (12), we solve for $\Delta I_f(s)$ as follows:

$$\Delta I_f(s) = \frac{x_{ad}(su_{d0} + u_{q0})}{x_f s(s^2+1)x'_d} \quad (15)$$

Solving the original functions of (13) and (15) according to the inverse Laplace transformation, we obtain the following:

$$\begin{cases} \Delta i_d(t) = u_{q0}/x'_d - (u_{q0}/x'_d)\cos t + (u_{d0}/x'_d)\sin t \\ \Delta i_q(t) = -u_{d0}/x_q + (u_{d0}/x_q)\cos t + (u_{q0}/x_q)\sin t \\ \Delta i_f(t) = \Delta i_d(t)(x_d - x'_d)/x_{ad} \end{cases} \quad (16)$$

Note that the non-attenuation of Δi_{dq} and Δi_f in (16) presupposes that the resistors R_a and R_f are neglected. Immediately, these resistors are introduced to describe the attenuation process of each component of the transient current.

Case 1: R_a is neglected and (13) can be simplified as follows:

$$\begin{cases} \Delta I_d(s) = \frac{(su_{d0}+u_{q0})(1+sT_f)}{s(s^2+1)(1+sT'_d)x_d}, \left(T_f = \frac{x_f}{r_f}, T'_d = T_f\frac{x'_d}{x_d}\right) \\ \Delta I_q(s) = \frac{su_{q0}-u_{d0}}{s(s^2+1)x_q} \end{cases} \quad (17)$$

where T_f and T'_d represent the excitation winding time constants for stator winding open circuit and short circuit, respectively. Solving for the roots of (17) is as follows:

$$s'_{(\Delta id)1,2,3,4} = 0, j, -j, -1/T'_d \text{ and } s'_{(\Delta iq)1,2,3} = 0, j, -j \quad (18)$$

These results show that only Δi_d has real roots, which implies that $-1/T'_d$ is the attenuation time constant of the dc component of id, while the dc component of Δi_q has no attenuation.

Case 2: R_f is neglected and (13) can be simplified as follows:

$$\begin{cases} \Delta I_d(s) = \frac{(R_a+sx_q)u_{d0}+x_q u_{q0}}{s\{[R_a+sx'_d(s)](R_a+sx_q)+x'_d(s)x_q\}} \\ \Delta I_q(s) = \frac{[R_a+sx'_d(s)]u_{q0}-x'_d(s)u_{d0}}{s\{[R_a+sx'_d(s)](R_a+sx_q)+x'_d(s)x_q\}} \end{cases} \quad (19)$$

Solving for the roots of (19) is as follows:

$$s''_{(\Delta idq)1,2} = -\frac{R_a(x'_d + x_q)}{2x'_d x_q} \pm j\sqrt{1 - \frac{R_a^2(x'_d - x_q)}{4x'_d x_q}} \quad (20)$$

The real part of this root corresponds to the attenuation time constant of the ac component of Δi_q. Let the attenuation time constant T_a be as follows:

$$T_a = |1/\text{Re}[s''_{(\Delta idq)1,2}]| = 2x'_d x_q/[R_a(x'_d + x_q)] \quad (21)$$

Next, as a supplement, we solve the real root of (13) and its corresponding original function which is the steady state value ($\Delta i_{dq\infty}$) of the DC component of the current (Δi_{dq}).

$$\Delta i_{d\infty} = \lim_{t\to\infty, s\to 0} \Delta I_d(s) = \frac{u_{q0}}{x_d} \text{ and } \Delta i_{q\infty} = \lim_{t\to\infty, s\to 0} \Delta I_q(s) = -\frac{u_{d0}}{x_q} \tag{22}$$

Combining (16), (17) and (21) to solve the transient current is shown below:

$$\begin{cases} \Delta i_d(t) = \underbrace{(u_{q0}/x'_d - u_{q0}/x_d)\exp(-t/T'_d) + u_{q0}/x_d}_{\text{DC component attenuation}} + \underbrace{[-(u_{q0}/x'_d)\cos t + (u_{d0}/x'_d)\sin t]\exp(-t/T_a)}_{\text{AC component attenuation}} \\ \Delta i_q(t) = -u_{d0}/x_q + [(u_{d0}/x_q)\cos t + (u_{q0}/x_q)\sin t]\exp(-t/T_a) \end{cases} \tag{23}$$

Finally, bring (5) into (23) to solve the full current equation as follows:

$$\begin{cases} i_d(t) = (u_{q0}/x'_d - u_{q0}/x_d)\exp(-t/T'_d) + E_{q0}/x_d \\ \quad +[-(u_{q0}/x'_d)\cos t + (u_{d0}/x'_d)\sin t]\exp(-t/T_a) \\ i_q(t) = [(u_{d0}/x_q)\cos t + (u_{q0}/x_q)\sin t]\exp(-t/T_a) \end{cases} \tag{24}$$

Converting the *d-q* coordinate to the *a-b-c* coordinate system, the result of the conversion is as follows:

$$\begin{cases} i_a(t) = [(\frac{U'_0}{x'_d} - \frac{U'_0}{x_d})\exp(\frac{-t}{T'_d}) + \frac{U_0}{x_d}]\cos(t+\theta_0) - \frac{U'_0(x_q+x'_d)}{2x'_d x_q}\exp(\frac{-t}{T_a})\cos\theta_0 \\ \quad -\frac{U'_0(x_q-x'_d)}{2x'_d x_q}\exp(\frac{-t}{T_a})\cos(2t+\theta_0) \\ i_b(t) = [(\frac{U'_0}{x'_d} - \frac{U'_0}{x_d})\exp(\frac{-t}{T'_d}) + \frac{U_0}{x_d}]\cos(t+\theta_0-\frac{2\pi}{3}) - \frac{U'_0(x_q+x'_d)}{2x'_d x_q}\exp(\frac{-t}{T_a})\cos(-\theta_0+\frac{2\pi}{3}) \\ \quad -\frac{U'_0(x_q-x'_d)}{2x'_d x_q}\exp(\frac{-t}{T_a})\cos(2t+\theta_0-\frac{2\pi}{3}) \\ i_c(t) = [(\frac{U'_0}{x'_d} - \frac{U'_0}{x_d})\exp(-t/T'_d) + \frac{U_0}{x_d}]\cos(t+\theta_0+\frac{2\pi}{3}) - \frac{U'_0(x_q+x'_d)}{2x'_d x_q}\exp(\frac{-t}{T_a})\cos(-\theta_0-\frac{2\pi}{3}) \\ \quad -\frac{U'_0(x_q-x'_d)}{2x'_d x_q}\exp(\frac{-t}{T_a})\cos(2t+\theta_0+\frac{2\pi}{3}) \end{cases} \tag{25}$$

Assuming empty load operation of the generator before pulsed load, combining (16), (17) and (21) can derive the excitation current (26) as follows:

$$i_f(t) = i_{f0} + \frac{x_d - x'_d}{U_0/i_{f0}}[\frac{U'_0}{x'_d}\exp(\frac{-t}{T'_d}) - \frac{U'_0}{x'_d}\exp(\frac{-t}{T_a})\cos t] \tag{26}$$

In summary, (25) and (26) describe the transient current characteristics of the generator during the period from no-load operation to pulsed load. Therefore, these equations also become the theoretical prerequisites for power prediction and impact load compensation in section below.

3. Power Prediction and Pulsed Load Compensation Strategies

Although the current responses of the SG from empty load to pulsed load were derived in the previous section, it was assumed in the analysis that the generator speed was constant. However, the mechanical and electromagnetic transients of the generator start at the same time, which leads to the fact that these current responses are accurate only for the first one or a few cycles. Therefore, the time allowed for prediction and compensation is also only one cycle after the pulse load is connected to the microgrid.

3.1. Description of Impulse Power Prediction Strategy

The equations in the previous section already contain all the information about the transient processes in the microgrid. Moreover, the prediction and compensation time has been set within one cycle (20 ms) in order to ensure that the assumption of constant rotational speed is valid.

First, the trigonometric and exponential functions are linearized to increase the speed of solving the equations. The linearization process is as follows:

$$\exp(-t/T'_d) \sim 1 - t/T'_d, \exp(-t/T_a) \sim 1 - t/T_a, t \to 0 \tag{27}$$

$$\cos(t+\alpha) \sim 1 - t^2/2, \cos(2t+\alpha) \sim 1 - 4t^2/2, t \to 0 \tag{28}$$

Note that the preconditions for (28) to be valid are such that

$$t + \alpha \to t, 2t + \alpha \to 2t \text{ as } t, \alpha \to 0$$

This means that theta is equal to 0, and $2/3\pi$ and $4/3\pi$ are required to make (28) satisfy linearization.

Bringing (28) into (25), and solving yields the value range of e as follows:

$$\theta_0 = \{0, 2\pi/3, 4\pi/3\} \tag{29}$$

Equation (29) shows that the i_a i_b and i_c in (26) can be satisfied simultaneously by at most two of them in the period at 50 Hz (20 ms). Therefore, in order to obtain the roots of the equation, (26) can be solved as a supplementary equation in conjunction with (25). The combined equations are as follows:

$$\begin{cases} \widehat{i}_a(t)\,|_{\theta_0=0} = [A(1-t/T'_d)+D](1-t^2/2) \\ \qquad +B(1-t/T_a)+C(1-t/T_a)(1-2t^2) \\ \qquad = \widehat{i}_b(t)\,|_{\theta_0=2\pi/3} = \widehat{i}_c(t)\,|_{\theta_0=4\pi/3} \\ \widehat{i}_f(t) = i_{f0} + E[(1-t/T'_d)-(1-t/T_a)(1-t^2/2)] \end{cases} \tag{30}$$

where

$$A = (\frac{U'_0}{x'_d} - \frac{U'_0}{x_d}), B = -\frac{U'_0(x_q + x'_d)}{2x'_d x_q}, C = -\frac{U'_0(x_q - x'_d)}{2x'_d x_q}, D = \frac{U_0}{x_d}, E = \frac{i_{f0}U'_0(x_d - x'_d)}{x'_d U_0}$$

Solving (30) obtains two time constants T'_d and T_a, respectively. Their expressions are given below

$$\begin{cases} \widehat{T'}_d = (Et(A(t^2-2)^2 + 4(B+C-2Ct^2)))/(4CE + 4Ci_{f0} \\ -8CEt^2 - 8Ci_{f0}t^2 + A(1+D)E(t^2-2)2 - 4Ei_{abc} \\ +2Et^2 i_{abc} + 4B(E + i_{f0} - i_f) - 4Ci_f + 8Ct^2 i_f) \\ \widehat{T}_a = (Et(A(t^2-2)^2 + 4(B+C-2Ct^2))]/[2(i_{f0} - i_f) \\ -A(t^2-2)(E(2+2D-t^2) \\ +4E(B+C-2Ct^2 - i_{abc}))) \end{cases} \tag{31}$$

Bringing (31) into (19) and (26), the expression containing the load estimate is constructed as follows:

$$\widehat{T'}_d = (x_f(x'_d + \widehat{x}))/(r_f(x_d + \widehat{x})) \tag{32}$$

$$\widehat{T}_a = (2(x'_d + \widehat{x})x_q)/((R_a + \widehat{R})(x'_d + \widehat{x} + x_q)) \tag{33}$$

where $\widehat{x}$ and $\widehat{R}$ represent the equivalent resistance and equivalent reactance of the impulse load, respectively.

By solving (27) for the $\widehat{x}$, the result is carried into (33) to obtain the $\widehat{R}$. Their expressions are as follows:

$$\begin{cases} \overset{\frown}{x} = (-r_f \overset{\frown}{T'}_d x_d + x'_d x_f)/(r_f \overset{\frown}{T'}_d - x_f)) \\ \overset{\frown}{R} = -R_a + (2(x'_d + \overset{\frown}{x})x_q)/(2\pi f \overset{\frown}{T}_a (x'_d + \overset{\frown}{x} + x_q)) \end{cases} \quad (34)$$

Finally, as a result, the power expression for the impulse load can be derived as follows:

$$\overset{\frown}{P} = 3U'_0 I'_0 \cos\varphi,\ \overset{\frown}{Q} = 3U'_0 I'_0 \sin\varphi,\ \varphi = \arctan(\overset{\frown}{x}/\overset{\frown}{R}) \quad (35)$$

3.2. Description of VSG-Based Load Compensation Strategy

Figure 1 Part II described the compensation device built based on a conventional VSG in this paper. This device includes an energy storage device, a voltage source inverter, and an LC filter. This generalized converter serves as compensation device, which not only verifies the correctness of the proposed compensation strategy but also ensures its universality. Therefore, the voltage and current loop controllers of the converter are the same as traditional VSC, with the addition of power droop and rotor mechanical characteristics. In overview, this section focuses on describing the proposed strategy and presents the VSG parameters and its control block diagram.

Figure 3 is the control block diagram of the VSG simulating the rotor mechanical characteristics of a synchronous machine. The equations described are as follows:

$$\begin{cases} J\omega \frac{d(\omega-\omega_0)}{dt} = P_{ref} - P_e - D(\omega-\omega_0) + \frac{1}{m}(\omega-\omega_0) \\ n(Q_{ref} - Q) + V_0 = V \end{cases} \quad (36)$$

where P and P_{ref} are the actual and desired values of the angular velocity of the virtual rotor, respectively. V and V_0 are the actual and desired values of the terminal voltage of the VSG. J is the virtual moment of inertia. D is the damping coefficient. T_m is the virtual mechanical input torque. T_e is the electromagnetic torque.

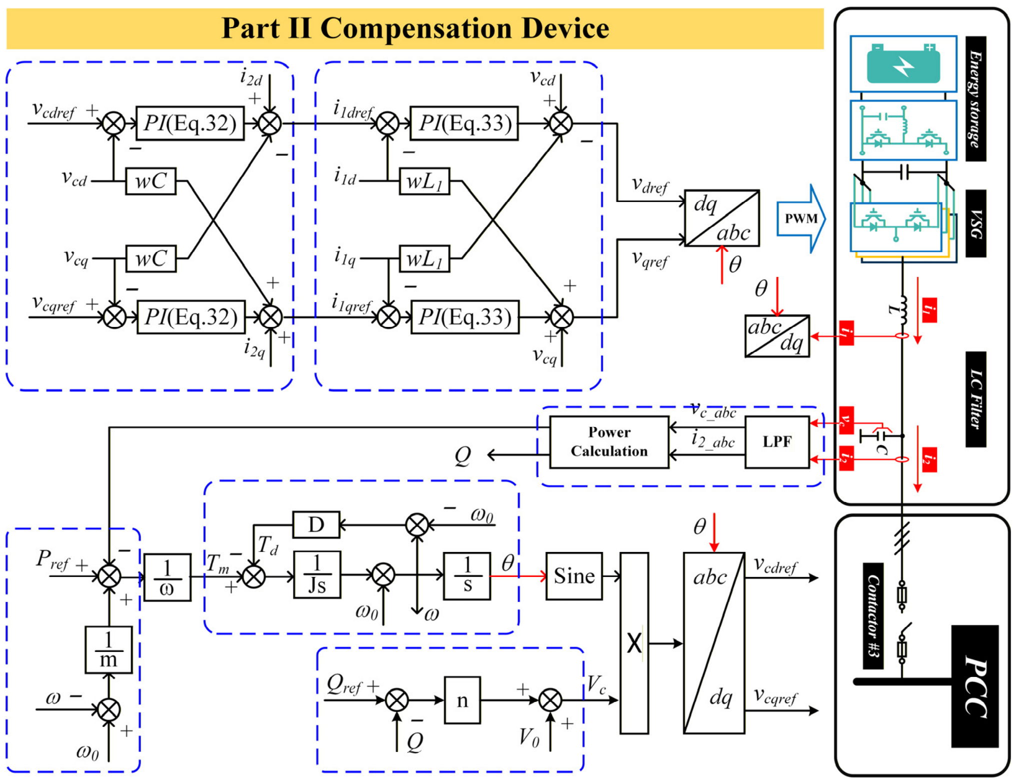

Figure 3. The control block diagram of the compensation device.

Figure 3 shows a control block diagram of the voltage and current loops of the VSG. These controllers are identical to conventional voltage source inverters; therefore, only the equations for their control loops are shown as follows:

$$\begin{cases} v_{dref} = (k_{pdv} + k_{idv}/s)(i_{1dref} - i_{1d}) - \omega L_1 i_{1q} + v_{cd} \\ v_{qref} = (k_{pqv} + k_{iqv}/s)(i_{1qref} - i_{1q}) + \omega L_1 i_{1d} + v_{cq} \end{cases} \tag{37}$$

where the subscripts d and q stand for the dq coordinate system. v_{dref} and v_{qref} are the desired values of the converter terminal voltage. i_{1d} and i_{1q} are the output currents of the converter. v_{cd} and v_{cq} are filter capacitor voltages. k_{pdv} and k_{idv} are controller parameters.

$$u_i^d = (k_{pdv} + \frac{k_{idv}}{s}) \cdot e_i^d = (k_{pdv} + \frac{k_{idv}}{s}) \cdot (i_{1dref} - i_{1d}), u_i^q = (k_{pdv} + \frac{k_{idv}}{s}) \cdot e_i^q = (k_{pdv} + \frac{k_{idv}}{s}) \cdot (i_{1dref} - i_{1d}),$$

u_i^d and u_i^q are current loop controller output signals.

$$\begin{cases} i_{1dref} = (k_{pdi} + k_{idi}/s)(v_{cdref} - v_{cd}) - \omega C v_{cq} + i_{2d} \\ i_{1qref} = (k_{pqi} + k_{iqi}/s)(v_{cqref} - v_{cq}) + \omega C v_{cd} + i_{2q} \end{cases} \tag{38}$$

where the subscripts d and q stand for the dq coordinate system. i_{1dref} and i_{1qref} are the desired values of the converter terminal voltage. i_{2d} and i_{2q} are the output currents of the VSG. k_{pdi} and k_{idi} are controller parameters.

$$u_v^d = (k_{pdi} + \frac{k_{idi}}{s}) \cdot e_v^d = (k_{pdi} + \frac{k_{idi}}{s}) \cdot (v_{cdref} - v_{cd}), u_v^q = (k_{pdi} + \frac{k_{idi}}{s}) \cdot e_v^q = (k_{pdi} + \frac{k_{idi}}{s}) \cdot (v_{cqref} - v_{cq}),$$

u_v^d and u_v^q are voltage loop controller output signals.

Combining (36)–(38) to build the controller of VSG can realize the power tracking control. The timing logic and algorithm structure of the power compensation strategy are shown in Figure 4 and Algorithm 1, respectively. Figure 4 shows the dynamic response of the three stages of the power compensation after the pulsed load is connected to the grid.

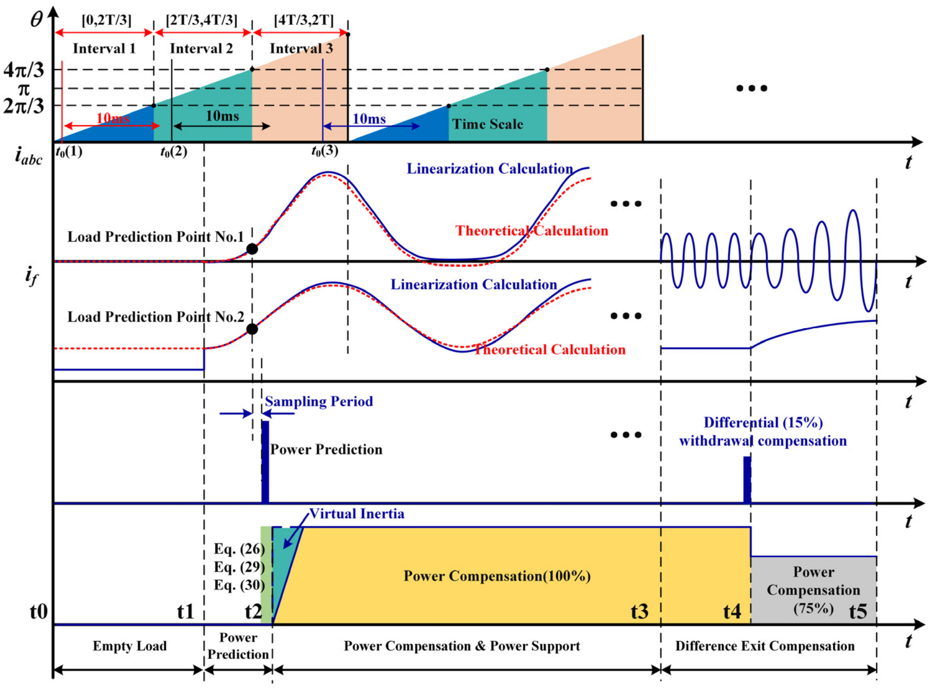

Figure 4. Timing logic diagram of the compensation strategy.

Stage 1 [t0–t1]: In this stage, the generator is operated with empty load and the PLL module realizes the voltage phase calculation.

Stage 2 [t1–t2]: At t1, the generator current is detected to be not equal to zero. It means that it enters into the power prediction process, at which time the controller starts to determine the voltage phase. At t2, θ is coincidentally equal to 0, $2\pi/3$, and $4\pi/3$; this means that the VSG completes the load power estimation.

Stage 3 [t2–t3]: At t2, VSG enters the process of power compensation. Note that the compensation power is equal to the estimated pulsed load power at this stage.

Stage 4 [t3–t5]: At t3, the excitation current does not change, which also means that the whole system is rebalanced. In this moment, we need to reduce the output power of the VSG by 20% and wait again for the excitation current to stabilize. Next, this process is repeated until the output power is equal to zero.

Algorithm 1. Power Compensation

```
PREDICT (P, Q)
  calculate A, B, C, D, E
  define N ⊂ R; Count ⊂ R
  θ(t) ← PLL for t = 1 ∗ ΔT, ..., n ∗ ΔT, ΔT = 40e − 6
  N = 0 ← {i_a ≠ 0||i_b ≠ 0||i_c ≠ 0}
  N + + ← {θ(t) ≠ 0||θ(t) ≠ 2π/3||θ(t) ≠ 4π/3}
  Count = N ← {θ(t) = 0||θ(t) = 2π/3||θ(t) = 4π/3}
  T_a, T'_d ← Equations (32) and (33)
  x̂, R̂ ← Equation (34)
  P̂, Q̂ ← Equation (35)
return P, Q;
```

According to Figure 4, the energy storage needs to fully support the unbalanced power of the grid at Stage 3. The power demand of energy storage is calculated as follows.

$$\begin{cases} W_1 = P_1 \cdot (t_3 - t_1) = P_1 \cdot t_S \\ W_2 = \sum\limits_{n=1}^{5} n \cdot (1 - n \cdot \eta) \cdot P_1 \cdot t_S \end{cases} \quad (39)$$

where t_s is the regulation time of SG. η is the power exit ratio of the energy storage device, and η is equal to 20% in this article. The transient response and step loading capability of the generator determines the capacity of the ESS. The regulation time of the DG for the SM is approximately equal to 0.5–1.5 ms. Therefore, the proposed strategy requires high capacity of ESS. Of course, exploring boundary conditions for generator regulation characteristics can minimize the need for capacity of ESS.

Algorithm 1 describes the control algorithm based on the STM32-DSP28379. and the program flow is described as follows:

Step 1: When the program flow enters the ADC interruption, the counter starts counting, and a phase-locked loop is used to estimate the voltage phase. In addition, A, B, C, D and E were calculated according to Equation (30).

Step 2: If a stator current value equal to zero is detected, the counter is cleared and the ADC interrupt is exited.

Step 3: If the stator current is not equal to zero, the counter starts counting until $\theta(t) = 0$, $\theta(t) = 2\pi/3$ or $\theta(t) = 4\pi/3$. Each time, the counter has a technical interval $\Delta T = 40e - 6s$.

Step 4: Substitute the above parameters into Equations (32)–(35) to calculate T_a, T'_d, $\widehat{x}, \widehat{R}$ and $\widehat{P}, \widehat{Q}$, respectively.

Step 5: The ADC interrupt exits and returns $\widehat{P}$ and $\widehat{Q}$.

In summary, the proposed compensation strategy utilizes the physical properties of the generator. Thus, this strategy allows the generator to go through the transient process according to its own regulation.

4. Result and Discussion

Figure 5 shows the experimental platform built according to the description of Figure 1, and the parameters of its main constituent elements are displayed in Table 2. Figure 5B shows the topology of the ship microgrid corresponding to the experimental platform. The inverter drives an asynchronous motor to simulate the prime motor characteristics. The asynchronous motor and the inverter are used to simulate the propulsion loads in the SM. IGBTs and resistors are used to simulate the pulsed loads. Firstly, the transient responses of pulsed load of the microgrid are verified in the built experimental environment. Secondly, the power prediction algorithm as well as the power compensation strategy after the pulse load is connected to the microgrid are verified. Finally, the correctness and effectiveness of the proposed strategies are discussed based on the obtained data and waveform. It should be clarified that this experimental platform builds a ship microgrid based on a power ratio of 1:200. This platform is able to verify the effectiveness and correctness of the proposed control strategy under the microgrid structure in Figure 5. Although the absolute time scales of the scaled-down simulated systems are different, the key dynamic processes of the systems are similar. In summary, the results in this work were obtained on a 30 kW experimental platform; although there is a gap between the power level and the actual ship/industrial microgrid, the conclusions revealed at the level of control methods have important theoretical value and engineering guidance. Figure 6 shows the waveform of the pulsed load accessed in the experiment, which is generated by driving the IGBT through PWM1, PWM2 and PWM3. The pulse period is equal to 200 ms, peak power is equal to 20 kW and duty cycle is equal to 80%.

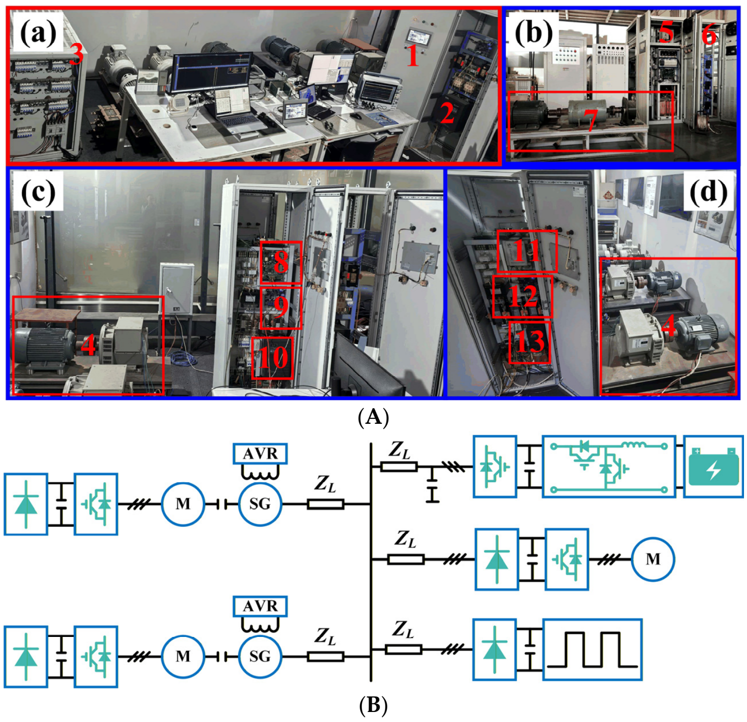

Figure 5. Experimental test platform. (**A**) (a) SM Platform Overview. (b) Energy storage compensation system. (c) #1 SM control system. (d) #2 SM control system. (1) PCC and synchronization controller. (2) Controllers for motor and rectified load. (3) Pulsed load. (4) Asynchronous motors and synchronous

generators. (5) VSG. (6) Supercapacitor energy storage device. (7) Motor and rectified load. (8) #1 AVR. (9) #1 synchronization controller. (10) #1 controller for simulating the speed characteristics of natural gas engines. (11) #2 AVR. (12) #2 synchronization controller. (13) #2 controller for simulating the speed characteristics of natural gas engines. (**B**) Topology diagram corresponding to the experimental platform.

Table 2. Parameters of the main elements of the microgrid.

Name	Parameter	Value	Unit
#1 SG & #2 SG	Rated Power	15	kW
	Rated Voltage	400	V
	ROCOF	0.5	Hz/s
#1 Converter & #2 Converter	Rated Power	20	kW
	Output Voltage	380	V
VSG	Output Power	30	kW
	Switching Frequency	10	kHz
	Filter Inductor	1	mH
	filter capacitor	20	uF

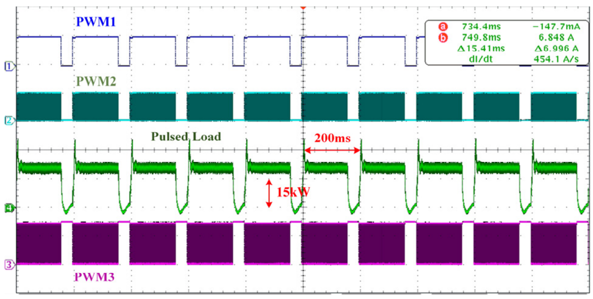

Figure 6. Power waveforms for pulsed loads. PWM1 drives a 10 kW pulsed load. PWM2 chopper driving a 3 kW pulse load, and PWM3 chopper driving a 2 kW pulse load. Oscilloscope horizontal axis represents 200 ms/div.

4.1. Analysis and Discussion of Transient Characteristics of Generator After Pulsed Load Connection

Figure 7 shows the transient response of the generator after connecting to the pulsed load when there is only one unit in the microgrid. Figure 7a,b,c respectively, show the current waveforms of the generator at different loading times. The value of θ not only contains the spatial position of the rotor but also reflects the loading time of the pulsed load during one cycle. Combining (a), (b) and (c), it can be seen that the difference in θ causes the difference in the transient waveform of the current. This conclusion and pattern is in high agreement with (25). This also means that θ is equal to 0, $2/3\pi$, and $4/3\pi$, corresponding to the simplest forms of calculation for *ia*, *ib* and *ic*, respectively. Figure 8 shows the transient response of the microgrid in the presence of two generators. The conclusions illustrated by it are similar to those shown in Figure 7.

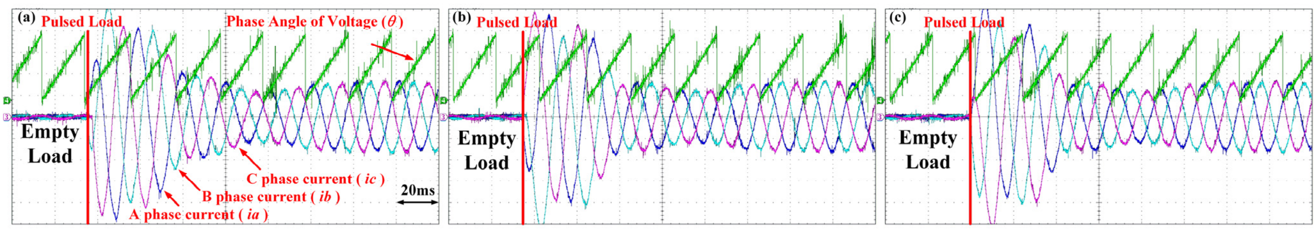

Figure 7. Transient response of a signal generator connected to the pulsed load. (**a**) $\theta \approx 1.256$. (**b**) $\theta \approx 3.454$. (**c**) $\theta \approx 5.966$. The green color represents the phase angle of voltage, the blue and magenta color represents the phase current.

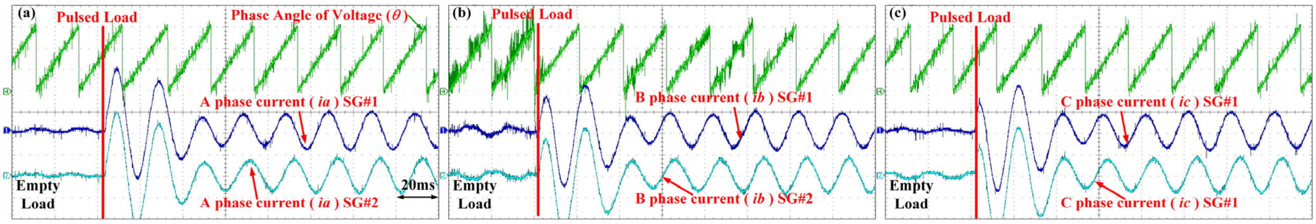

Figure 8. Transient response of a dual generator connected to the pulse load. (**a**) $\theta \approx 3.266$. (**b**) $\theta \approx 1.570$. (**c**) $\theta \approx 2.826$. The green color represents the phase angle of voltage, the blue color represents the phase current.

The transient waveforms of the excitation voltage and current of the generator excitation are shown in Figure 9. Figure 9a–c shows the transient response of a generator under pulsed load, while Figure 9d shows the transient response of two generators under pulsed load. It can be seen from Figure 9 that the excitation voltage, excitation current and stator current will change with the change in theta, which verifies the rationality of (26). Specifically, the excitation current and excitation voltage of each generator will change due to the impulse load in microgrid. Therefore, impulse load prediction can be achieved by combining changes in theta, stator current, and excitation current. This result provides a prerequisite for the realization of "proactive" power compensation in microgrids.

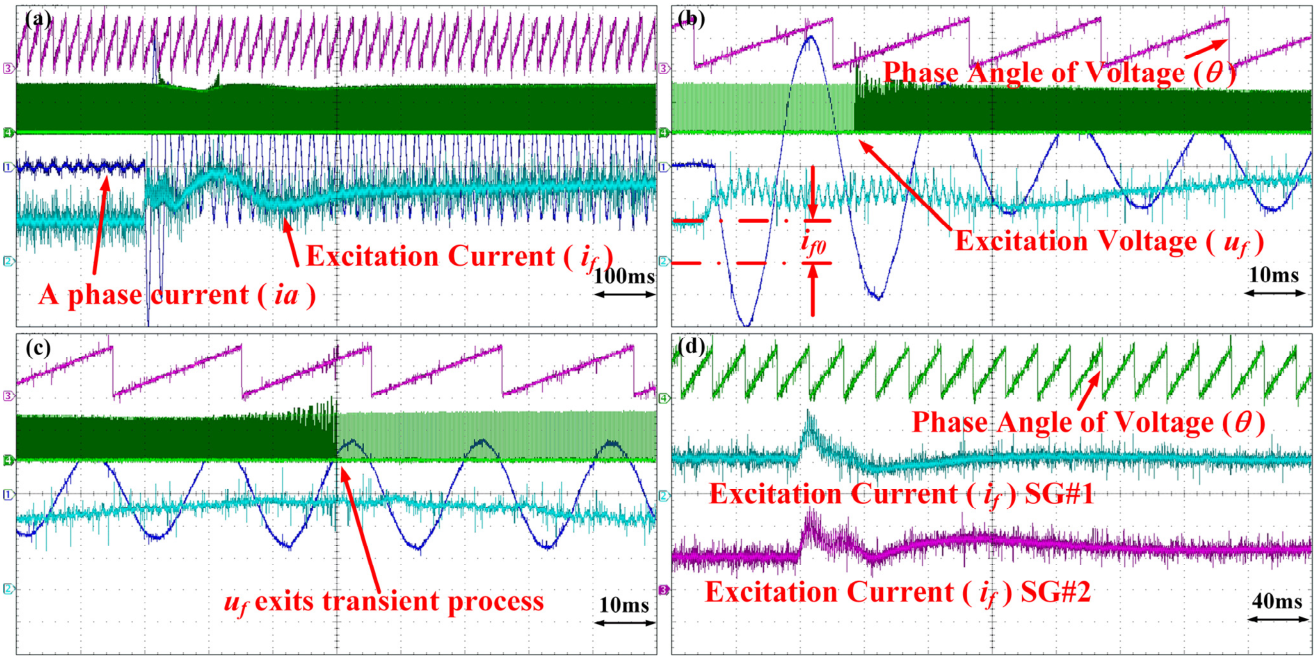

Figure 9. Transient response of the microgrid after the connected pulsed load. (**a**) Load connection moments. (**b**) Transient regulation process. (**c**) Exit transient process. (**d**) Excitation current response of the dual sets. The violet color represents the phase angle of voltage, the blue color represents the excitation current, the navy blue color represents the phase current.

4.2. Analysis and Discussion of Power Prediction and Compensation Characteristics

Figure 10 shows the transient response of the two generator systems after the microgrid is connected to the pulsed load. It contains the excitation current, stator current and power prediction signals. Note that θ is used as a timeline in the figure to determine the timing of the overall dynamic response. Figure 10a,b show the respective transient responses of the two generators after the microgrid is suddenly connected to a 20 kW pulsed load, respectively.

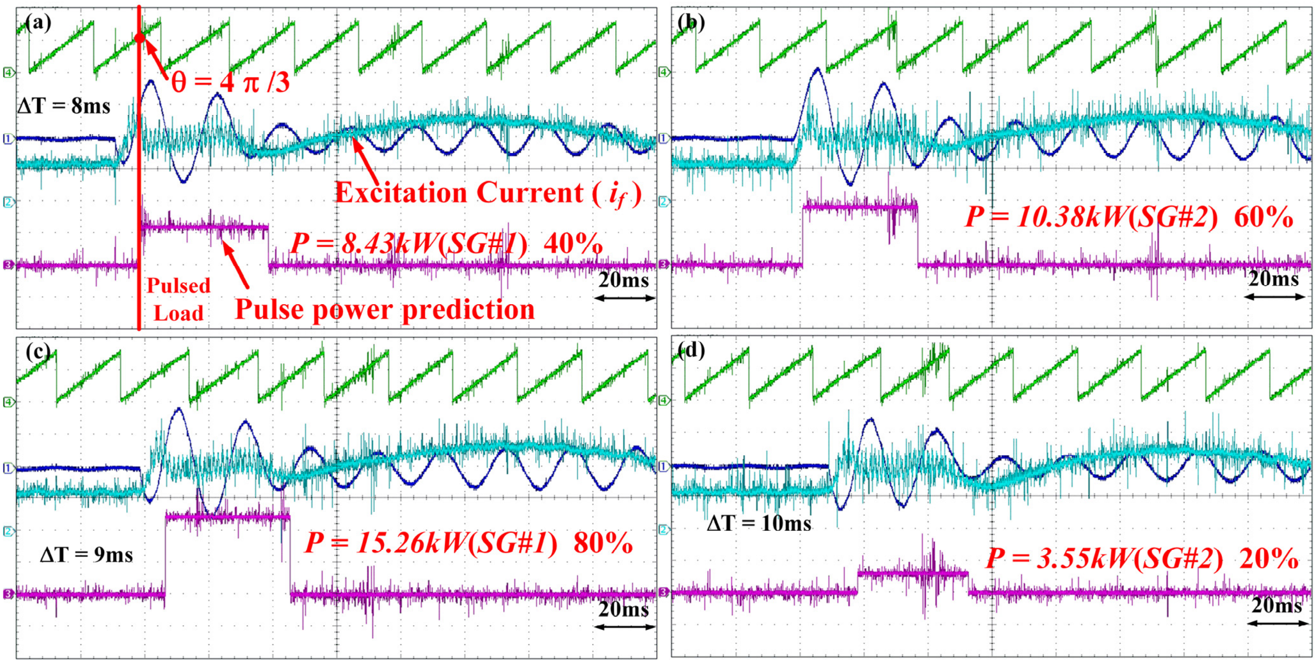

Figure 10. Transient response and pulsed load prediction for two generators. (**a**) The #1 SG distributes 40% of the pulsed power. (**b**) The #2 SG distributes 60% of the pulsed power. (**c**) The #1 SG distributes 80% of the pulsed power. (**d**) The #1 SG distributes 20% of the pulsed power. The violet color represents the predictive signals, the blue color represents the excitation current, the navy blue color represents the phase current, the green color represents the phase angle of voltage.

As can be seen from Figure 10a,b, the transient waveforms of each generator are used to calculate their individual load power when the pulsed load is connected to the microgrid. As a result, Figure 10a,b demonstrate that both generator systems achieve power prediction within 10 ms of pulsed load connection. This conclusion not only validates the correctness of (29) but also demonstrates that the time scale of 10 ms can guarantee the accuracy of load forecasting. Figure 10c,d serve as a control group with access to the pulse load which is equal to 20 kW, and the conclusions demonstrated are the same as the previous results. Overall, the phenomena depicted in Figures 4 and 10 are in good agreement with the inferences. It should be added that the time scale of 10 ms ensures that the magnetic field of the generator rotor coincides precisely with one of the A, B and C axis after loading. It is this physical property that allows the prediction equations to be treated in a linearized manner. The dynamic performance of the proposed algorithm and the existing work is comparatively analyzed in Table 1. The proposed algorithm is capable of predicting the power of the pulsed load within 4–20 ms. Since the algorithm mainly locks three time points within 20 ms for equation simplification, the stability and robustness of the algorithm need further analysis.

Figure 11 shows the excitation current waveforms of the two generators and the output power waveforms of the VSG after the microgrid is connected to a 20 kW pulse load. The graph shows that the VSG starts to output power 20 ms after the pulsed load is connected to the microgrid. The expected value of the output power of the VSG is approximately equal to the instantaneous power of the pulse load. This means that from the time the pulse load enters the microgrid, the microgrid will be rebalanced in 28 ms according to Figure 11.

To summarize, the compensation power in this compensation strategy is no longer subject to closed-loop control in accordance with the current variations in the power grid. Essentially, during the generator transient, the VSG rapidly injects the differential power into the microgrid. This not only rebalances the power of the microgrid but also allows the microgrid to rapidly transition from transient to steady state. It is necessary to add that the reasons for the limitations of the proposed algorithm can be discussed as follows: (1) In the program flow depicted in Algorithm 1, there are only three moments when $\theta(t) = 0$, $\theta(t) = 2\pi/3$ or $\theta(t) = 4\pi/3$ to start the power calculation after the pulse load is connected, so the algorithm has a high dependence on the accuracy of the parameters. (2) The excitation parameters of the SG are needed. In order to ensure the delay of the ADC interruption, it is required that the parameters of the excitation system in the AVR can be transferred to the controller through faster communication. For example, TCP communication is chosen in this paper. (3) The proposed algorithm applies to a SM whose constituent units are highly controllable and whose load characteristics are known. This is in contrast to a general microgrid, which requires more integrated control.

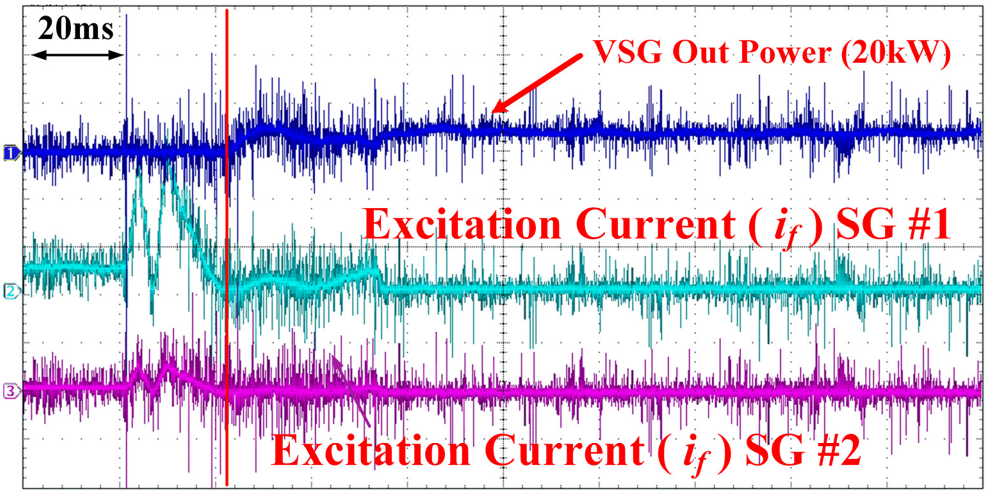

Figure 11. Compensation power of VSG and excitation current of two generators.

5. Conclusions

In this paper, a microgrid proactive power compensation strategy for pulsed load is proposed and implemented. This strategy aims to allow a generator or microgrid to achieve transient ride-through within 10 ms. In comparison with the traditional compensation strategy, the proposed compensation strategy is not a passive power compensation based on the variation in generator current, but a proactive injection of differential power into the microgrid based on the load power at the moment of perturbation. After the microgrid achieves transient state, VSG exits from compensation in batches according to a certain percentage. Therefore, the compensation process is passively regulated and followed by the generator set according to its own physical characteristics under the proactive guidance of the VSG output power. The results and experimental discussion of this paper are summarized as follows.

Firstly, SMs have a variety of power electronic loads compared to ordinary microgrids. As a result, these pulsed loads cause more harm to the stability of the SM. The proposed control strategy uses a transient model of the generator to determine and predict the type of pulsed load, reducing the minimum time scale over which the generator can respond to the pulsed load. Second, this algorithm requires that all state quantities of the SM can be captured, and it is therefore currently only applicable to highly centralized control of SM.

Although the proposed strategy has realized proactive power compensation for pulsed loads, the algorithm involves several sampling links, such as excitation voltage, stator current generator response parameters and so on. Therefore, the influence of sensor accuracy on the proposed strategy cannot be ignored, and the robustness of the algorithm is also a direction for further research.

Author Contributions: Y.D.: Conceptualization, Methodology, Investigation, Formal analysis, Validation, Visualization, Writing—Original draft, Data curation; K.Z. (corresponding author): Supervision, Project administration, Funding acquisition, Resources, Writing—Review and editing, Validation; J.D.: Methodology, Software, Investigation; L.S., Formal analysis, Resources. All authors have read and agreed to the published version of the manuscript.

Funding: This research was funded by the China National Natural Science Foundation Grant No. 52177211 and Heilongjiang Postdoctoral Research Starting Foundation Grant No. LBH-Q20020.

Data Availability Statement: Dataset available on request from the authors. The raw data supporting the conclusions of this article will be made available by the authors on request.

Conflicts of Interest: The authors declare no conflicts of interest.

References

1. Feng, Z.; Wei, F.; Wu, C.; Sui, Q.; Lin, X.; Li, Z. Novel Source-Storage Coordination Strategy Adaptive to Impulsive Generation Characteristic Suitable for Isolated Island Microgrid Scheduling. *IEEE Trans. Smart Grid* **2023**, *14*, 3791–3803. [CrossRef]
2. Yang, B.; Li, H.; Xu, S.; Liu, H.; Lu, S. Systematic Methods to Eliminate the Transient Circulating Powers in the Multi-VSGs System. *IEEE Trans. Smart Grid* **2024**, *15*, 179–190. [CrossRef]
3. Moran-Rio, D.P.; Roldan-Perez, J.; Prodanovic, M.; Garcia-Cerrada, A. Influence of the Phase-Locked Loop on the Design of Microgrids Formed by Diesel Generators and Grid-Forming Converters. *IEEE Trans. Power Electron.* **2022**, *37*, 5122–5137. [CrossRef]
4. Gong, Q.; Xu, J.; Ye, J.; Feng, H.; Shen, A. Nonlinear Model Predictive Control for Premixed Turbocharged Natural Gas Engine. *IEEE/ASME Trans. Mechatron.* **2022**, *27*, 3694–3705. [CrossRef]
5. Liu, J.; Yang, F.; Wang, H.; Ouyang, M.; Hao, S. Effects of pilot fuel quantity on the emissions characteristics of a CNG/diesel dual fuel engine with optimized pilot injection timing. *Appl. Energy* **2013**, *110*, 201–206. [CrossRef]
6. Lebedevas, S.; Pukalskas, S.; Daukšys, V.; Rimkus, A.; Melaika, M.; Jonika, L. Research on Fuel Efficiency and Emissions of Converted Diesel Engine with Conventional Fuel Injection System for Operation on Natural Gas. *Energies* **2019**, *12*, 12. [CrossRef]
7. Habibi, S.I.; Sheikhi, M.A.; Khalili, T.; Abadi, S.A.G.K.; Bidram, A.; Guerrero, J.M. Multiagent-Based Nonlinear Generalized Minimum Variance Control for Islanded AC Microgrids. *IEEE Trans. Power Syst.* **2024**, *39*, 316–328. [CrossRef]
8. Liu, J.; Xia, Y.; Wei, W.; Feng, Q.; Yang, P. Effect of Control Damping on Small-Signal Stability of Grid-Forming VSCs Considering Interaction Between Inner and Outer Loops. *IEEE Trans. Power Electron.* **2024**, *39*, 7685–7695. [CrossRef]
9. Li, X.; Feng, P.; Tian, Z.; Huang, M.; Shu, S.; Zha, X.; Hu, P. Transient Stability Analysis for Grid-Tied VSG Considering High-Order Nonlinear Interactions Between Active and Reactive Power Control Loops. *IEEE Trans. Power Electron.* **2024**, *39*, 6974–6988. [CrossRef]
10. Lu, J.; Zhang, B.; Hou, X.; Guerrero, J.M. A Distributed Control Strategy for Unbalanced Voltage Compensation in Islanded AC Microgrids Without Continuous Communication. *IEEE Trans. Ind. Electron.* **2023**, *70*, 2628–2638. [CrossRef]
11. Liu, X.; Shahidehpour, M.; Li, Z.; Liu, X.; Cao, Y.; Tian, W. Protection Scheme for Loop-Based Microgrids. *IEEE Trans. Smart Grid* **2017**, *8*, 1340–1349. [CrossRef]
12. Zheng, H.; Liu, Z.; An, R.; Liu, J.; Wu, T.; Lin, Z. An Islanding Detection Method Using Synchronized Small-AC-Signal Injection for Grid-Forming Inverters in Microgrids. *IEEE Trans. Power Electron.* **2023**, *38*, 5816–5831. [CrossRef]
13. Yu, H.; Lyu, J.; Cai, X. High-Frequency Self-Stabilizing Control for a Grid-Tied VSC. *IEEE Trans. Power Electron.* **2024**, *39*, 7980–7994. [CrossRef]
14. Mohammed, N.; Lashab, A.; Ciobotaru, M.; Guerrero, J.M. Accurate Reactive Power Sharing Strategy for Droop-Based Islanded AC Microgrids. *IEEE Trans. Ind. Electron.* **2023**, *70*, 2696–2707. [CrossRef]
15. Ke, S.; Yang, J.; Chen, L.; Fan, P.; Shi, X.; Li, G.; Wu, F. A Frequency Control Strategy for EV Stations Based on MPC-VSG in Islanded Microgrids. *IEEE Trans. Ind. Inform.* **2024**, *20*, 1819–1831. [CrossRef]
16. Chen, S.; Sun, Y.; Hou, X.; Han, H.; Fu, S.; Su, M. Quantitative Parameters Design of VSG Oriented to Transient Synchronization Stability. *IEEE Trans. Power Syst.* **2023**, *38*, 4978–4981. [CrossRef]
17. Behera, S.K.; Panda, A.K.; Naik N, V.R. An Adaptive Control Approach for Improved Power Quality and Power Ripple Mitigation in a Self-Synchronized Grid-Tied VSG. *IEEE Trans. Ind. Electron.* **2025**, *72*, 3664–3675. [CrossRef]
18. Wang, M.; Yang, Y.; Zhang, Y.; Ambia, M.N. Grid Impedance Adaptive VSG Control Based on Accurate Small-Signal Modelling. *IEEE Trans. Ind. Appl.* **2025**, *61*, 5891–5903. [CrossRef]
19. Chen, S.; Sun, Y.; Han, H.; Fu, S.; Luo, S.; Shi, G. A Modified VSG Control Scheme With Virtual Resistance to Enhance Both Small-Signal Stability and Transient Synchronization Stability. *IEEE Trans. Power Electron.* **2023**, *38*, 6005–6014. [CrossRef]
20. Li, G.; Song, W.; Liu, X. A Quasi-Harmonic Voltage Feedforward Control for Improving Power Quality in VSG-Based Islanded Microgrid. *IEEE J. Emerg. Sel. Top. Power Electron.* **2024**, *12*, 2994–3004. [CrossRef]

21. Liu, Y.; Wang, Y.; Wang, M.; Xu, Z.; Peng, Y.; Li, M. Coordinated VSG Control of Photovoltaic/Battery System for Maximum Power Output and Grid Supporting. *IEEE J. Emerg. Sel. Top. Circuits Syst.* **2022**, *12*, 301–309. [CrossRef]
22. Fu, S.; Sun, Y.; Lin, J.; Chen, S.; Su, M. P/Q-ω/V Admittance Modeling and Oscillation Analysis for Multi-VSG Grid-Connected System. *IEEE Trans. Power Syst.* **2023**, *38*, 5849–5859. [CrossRef]
23. Heins, T.; Joševski, M.; Karthik Gurumurthy, S.; Monti, A. Centralized Model Predictive Control for Transient Frequency Control in Islanded Inverter-Based Microgrids. *IEEE Trans. Power Syst.* **2023**, *38*, 2641–2652. [CrossRef]